Phase-Shifting Zernike Interferometer Wavefront Sensor

J. Kent Wallace*[,a], Shanti Rao[a], Rebecca M. Jensen-Clem[b], Gene Serabyn[a]
[a]Jet Propulsion Laboratory, California Institute of Technology, 4800 Oak Grove Drive, Pasadena, CA, USA 91109
[b]Massachusetts Institute of Technology, 77 Massachusetts Ave., Cambridge, MA, USA 02139

ABSTRACT

The canonical Zernike phase-contrast technique[1,2,3,4] transforms a phase object in one plane into an intensity object in the conjugate plane. This is done by applying a static $\pi/2$ phase shift to the central core ($\sim \lambda/D$) of the PSF which is intermediate between the input and output planes. Here we present a new architecture for this sensor. First, the optical system is simple and all reflective. Second, the phase shift in the central core of the PSF is dynamic and or arbitrary size. This common-path, all-reflective design makes it minimally sensitive to vibration, polarization and wavelength. We review the theory of operation, describe the optical system, summarize numerical simulations and sensitivities and review results from a laboratory demonstration of this novel instrument.

Keywords: Wavefront sensing, Zernike phase-contrast, adaptive optics.

1. INTRODUCTION

Zernike's method of phase-contrast was transformative for the biological sciences, for it allowed biological specimens in aqueous solutions to be viewed for the first time not as intensity objects, but instead as phase objects. The amplitude of the light passing through these essentially transparent media (the aqueous solution and the cells, for instance) was unaffected, and thus the specimen was indistinguishable from its surroundings. However, the index of refraction is distinctly different, and phase-contrast permitted these phase objects to be viewed as intensity objects. It is for this work that Zernike was awarded the Nobel Prize in 1953.

Dicke[5] first proposed that the phase-contrast method could be employed for wavefront sensing in an adaptive optics system. In a similar manner, the index of refraction variations of the turbulent atmosphere leave the electric field amplitude primarily unaffected but create large phase errors. A Zernike wavefront sensor (ZWFS) would turn the phase errors into easily measured amplitude errors. But the Zernike wavefront sensor has other distinct advantages. For instance, the ZWFS measures the electric field phase directly. In comparison, the Shack-Hartmann wavefront sensor (SHWFS) reconstructs the phase by first measuring the phase gradient and then numerically integrating it. This process is susceptible to noise propagation, particularly in the lowest spatial frequency modes. The ZWFS, because it measures phase directly, does not suffer from this problem.

However, the classical static Zernike has other limitations. Given that the intensity of the output pupil is interpreted as phase, any noise source that generates an intensity measurement error will lead to an erroneous estimate of the phase. For instance, any light that is scattered (like a glint internal to the optical train) would lead to an intensity variation which in turn would be misinterpreted as phase in the input pupil. In the new architecture described in this paper, the static phase shift (say $\pi/2$) in the PSF is replaced by a dynamic and variable phase shift (nominally $-\pi/2$, 0, $+\pi/2$, and $+\pi$). This diversity in the phase allows the intensity images to be demodulated such that the phase and amplitude of the electric field can be determined independently. Likewise, any part of the intensity measurement that is not also modulated by these phase shifts is rejected in the reconstruction process which makes the sensor insensitive to issues such as scattered light and glints as well as noise sources in the detection process (like detector noise) that is not synchronous with the phase modulation.

*James.K.Wallace@jpl.nasa.gov; phone 1 818 393-7066; fax 1 818 393-3290; jpl.nasa.gov

2. PRINCIPLES OF ZERNIKE PHASE-CONTRAST

The following discussion of Zernike phase contrast can be found in many optical textbooks[6,7,8,9,10]. The purpose of including it here is to demonstrate the simplicity with which the phase can be reconstructed using the Zernike WFS. The input pupil, image plane, and output pupil refer to the optical system represented in Figure 1.

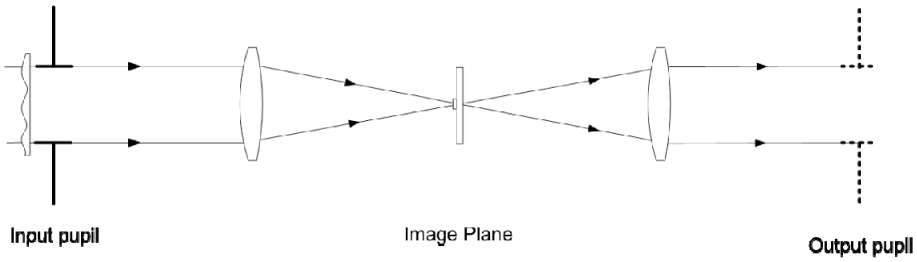

Figure 1. The canonical optical system used to illustrate Zernike phase contrast.

The electric field immediately before the input pupil is given by

$$E(u,v) = P(u,v) \cdot A(1+\varepsilon(u,v))e^{i\phi(u,v)} \tag{1}$$

where *P(u,v)* is the pupil function, *A* is the mean electric field amplitude, *ε(u,v)* is the point-by-point variation in the electric field amplitude, and *ϕ (u,v)* is the pupil-dependent phase. Assuming that *ϕ(u,v)* is small compared to a radian, the exponential term is expanded in a Taylor Series to first order. After all second order terms are dropped, the electric field is now given by

$$E(u,v) \approx P(u,v) \cdot A(1+\varepsilon(u,v)+i\phi(u,v)). \tag{2}$$

The electric field at the pupil plane, given by Equation 2, is propagated to the image plane by a Fourier transform, represented by Equation 3:

$$E(\eta,\upsilon) = F[P(u,v)] * F[A(1+\varepsilon(u,v)+i\phi(u,v))] \tag{3}$$

where *F*[] represents the Fourier transform, the Cartesian coordinates at the image plane are given by η and ν, and the convolution is represented by the * symbol. If the Fourier transform of the pupil function is represented by an amplitude point spread function, indicated here by PSF, Equation 3 is simplified to

$$E(\eta,\upsilon) = APSF(\eta,\upsilon) + APSF(\eta,\upsilon) * F[\varepsilon(u,v)+i\phi(u,v)]. \tag{4}$$

In the simplified case, a uniform phase shift of magnitude θ is applied to the central image plane PSF, giving a phase-shifted electric field:

$$E(\eta,\upsilon) = APSF(\eta,\upsilon)e^{i\theta} + APSF(\eta,\upsilon) * F[\varepsilon(u,v)+i\phi(u,v)]. \tag{5}$$

Equation 5 is Fourier transformed to represent the electric field in the output pupil plane coordinates x and y:

$$E(x,y) = AP(x,y) \cdot (e^{i\theta} + \varepsilon(x,y) + i\phi(x,y)). \tag{6}$$

The re-imaged electric field represented in the output pupil by Equation 6 differs from the input pupil plane electric field in Equation 2 in that the DC part of the electric field, has been replaced by a phase-shifted version. Because the remaining expressions deal only with the output pupil plane, the explicit pupil notation *P(x,y)* and the coordinate notation are dropped hereafter.

Given an image plane phase shift of θ = -π/2, the output pupil electric field and intensity are given by

$$E = A(e^{-i\pi/2} + \varepsilon + i\phi) = A(-i + \varepsilon + i\phi) \tag{7}$$

$$I = E \cdot E^* = A^2(1+\varepsilon^2 - 2\phi + \phi^2)\,. \tag{8}$$

This "static," or single phase shift, method of Zernike phase reconstruction has several advantages. First, the measurements are easy to interpret without complicated mathematics. Second, the process is common mode. Third, the sampling of the image plane is easy to control by placing a zoom lens in front of the output pupil viewing camera. The major disadvantage of the static approach, however, lies in the noise response: any system error resulting in intensity changes in the output pupil is interpreted as a phase error. Errors introduced by stray light, dark current, etc. therefore play a significant role in the static Zernike error budget.

In order to overcome this disadvantage, we propose the "dynamic" Zernike sensor. In the dynamic approach, multiple phase shifts are applied at the image plane, and the resulting intensity modulated signals are demodulated in post-processing. This dynamic phase shifting has the effect of rejecting noise sources that are not synchronous with the phase step.

If four different phase shifts between -λ/4 and λ/2, in quarter-wave steps, (θ= -π/2, 0, π/2 , π) are introduced at the image plane, Equation 6 can be re-expressed as

$$\begin{aligned} E_1 &= A(e^{-i\pi/2} + \varepsilon + i\phi) = A(-i + \varepsilon + i\phi) \\ E_2 &= A(e^{i0} + \varepsilon + i\phi) = A(1 + \varepsilon + i\phi) \\ E_3 &= A(e^{i\pi/2} + \varepsilon + i\phi) = A(i + \varepsilon + i\phi) \\ E_4 &= A(e^{-i\pi} + \varepsilon + i\phi) = A(-1 + \varepsilon + i\phi) \end{aligned} \tag{9}$$

and their corresponding intensities as

$$\begin{aligned} I_1 &= E_1 \cdot E_1^* = A^2(1+\varepsilon^2 - 2\phi + \phi^2) \\ I_2 &= E_2 \cdot E_2^* = A^2(1+\varepsilon^2 + 2\varepsilon + \phi^2) \\ I_3 &= E_3 \cdot E_3^* = A^2(1+\varepsilon^2 + 2\phi + \phi^2) \\ I_4 &= E_4 \cdot E_4^* = A^2(1+\varepsilon^2 - 2\varepsilon + \phi^2) \end{aligned} \tag{10}$$

where E^* represents the complex conjugate of E. These four intensity measurements can be combined to estimate the phase and amplitude errors of the electric field at the input pupil:

$$\phi = \frac{I_3 - I_1}{4I_0} \tag{11}$$

$$\varepsilon = \frac{I_2 - I_4}{4I_0} \tag{12}$$

Therefore, the phase and amplitude errors can be estimated by differencing and normalizing the intensities measured at the output pupil. The I_0 term represents the normalization term, and to first order it is the intensity in the output pupil in the absence of amplitude and phase errors. It can be estimated as $I_0 = (I_1 + I_2 + I_3 + I_4)/4$.

This dynamic approach improves upon the static approach in that it rejects all sources of noise not common with the phase-shifting frequency, such as detector noise and stray light. Because it is common mode, the method is insensitive to non-common path optics, polarization, vibration, and thermal drift. Because the sensor is all-reflective, it works with broadband light.

2.1 Sensitivity to a static phase offset

We now explore the effect of having a phase offset from the nominal phase stepping positions. This corresponds to having the capillary and filament slightly non-coplanar when we think the phase step, θ, is zero. This is modeled mathematically by adding an offset phase term, given by δ, in equations 9.

$$\begin{aligned} E_1 &= A(e^{-i\pi/2+\delta} + \varepsilon + i\phi) \\ E_2 &= A(e^{i0+\delta} + \varepsilon + i\phi) \\ E_3 &= A(e^{i\pi/2+\delta} + \varepsilon + i\phi) \\ E_4 &= A(e^{-i\pi+\delta} + \varepsilon + i\phi) \end{aligned} \tag{13}$$

As before, the corresponding intensities are given by the follow:

$$\begin{aligned} I_1 &= E_1 \cdot E_1^* = A^2(1+\varepsilon^2+\phi^2 - 2\phi Cos(\delta) + 2\varepsilon Sin(\delta)) \\ I_2 &= E_2 \cdot E_2^* = A^2(1+\varepsilon^2+\phi^2 + 2\phi Sin(\delta) + 2\varepsilon Cos(\delta)) \\ I_3 &= E_3 \cdot E_3^* = A^2(1+\varepsilon^2+\phi^2 + 2\phi Cos(\delta) - 2\varepsilon Sin(\delta)) \\ I_4 &= E_4 \cdot E_4^* = A^2(1+\varepsilon^2+\phi^2 - 2\phi Sin(\delta) - 2\varepsilon Cos(\delta)) \end{aligned} \tag{14}$$

If we use our same algorithms from equations 11 and 12, we get the following expressions:

$$\widehat{\phi} = \frac{I_3 - I_1}{4A^2} = \phi Cos(\delta) - \varepsilon Sin(\delta) \tag{15}$$

$$\widehat{\varepsilon} = \frac{I_2 - I_4}{4A^2} = \varepsilon Cos(\delta) + \phi Sin(\delta) \tag{16}$$

The effect of a constant phase offset is that the phase and amplitude errors can 'rotate' into each other. If the zero phase point is off by λ/4, or 160 nm for λ = 635 nm, then $\phi = -\varepsilon$, and $\varepsilon = \phi$. Dynamic errors in the phase step will cause the same effect of 'rotating' phase errors into amplitude errors, and amplitude errors into phase errors. For small offset errors, equations 15 and 16 can be simplified as follows:

$$\widehat{\phi} - \phi \approx -\varepsilon\,\delta \tag{17}$$

$$\widehat{\varepsilon} - \varepsilon \approx +\phi\,\delta \tag{18}$$

3. EXPERIMENTAL SETUP

3.1 Testbed Overview

In order to demonstrate the capabilities of the dynamic Zernike wavefront sensor in the lab, a hardware testbed was constructed to introduce and measure known phase errors. The testbed is shown schematically in Figure 2.

Light enters the system from the upper right in Figure 2 through the input pupil. In this plane, we place different phase aberrations. These phase-plate aberrations have been quantified separately with a Zygo interferometer and allow us to quantify the performance of our sensor. The input pupil is located at the focal length of the parabola; the pupil is imaged to infinity by the parabola (the system is telecentric), and the light passing through the pupil is imaged to the focal plane. The focal plane has a custom optical assembly that is composed of an optical capillary tube internal to which is a small, phase-shifting micro mirror which will be described next. This micro mirror imposes a phase shift only to the core of the PSF. The phase of the light outside of the filament is not phase-shifted. Both of these electric fields then reflect from this assembly back to the parabola. The micro mirror position is driven by a PZT whose motion is controlled via a computer interface. Upon reflection, a real image of the pupil is formed again at the focal length of the parabola. This real image is

them relayed to the pupil viewing camera (a CCD). Frame acquisition is made synchronous with the PZT motion with custom software which controls both. These intensity frames correspond to the four intensity images in equation 10.

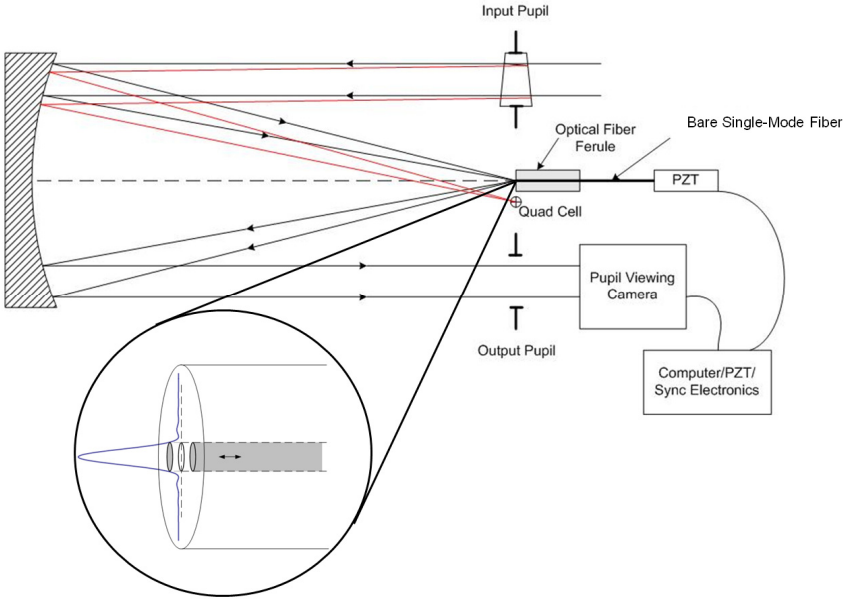

Figure 2. Simplified diagram of the Dynamic Zernike instrument which illustrates the key components. Light first enters the system from the upper right through the input pupil. In this pupil, which is located at the focal length of the parabola, are placed transparent phase aberrations which have been measured separately. This beam is focused by the parabola to the custom assembly in the focal plane. This assembly consists of a optical fiber ferrule inside of which is a bare single mode fiber. They are end polished and silver coated. The optical filament moves in the ferrule and imparts a phase shift to the core of the PSF. This beam then reflects back to the OAP where, upon reflection a real image of the pupil is formed. This pupil is then viewed with the CCD camera.

3.2 Focal Plane Assembly

The capillary is a borosilicate glass which has been end polished such that the face is optically flat and normal to the axis of symmetry to within an arcminute. The capillary hole size is on the order of 127 um. The bare single mode fiber has been stripped of its acrylate coating. It is then acid etched in hydrofluoric acid to reduce its diameter from a nominal 126 um, to ~122 um. Once installed into the capillary tube, its end faces are cleaved. This assembly is coated with a metallic coating to provide high reflectivity in the visible and near infrared. The shadowing that occurs of the edge of the filament is not significant in terms of its impact when the face of the fiber filament is near the face of the capillary.

In the experiment, the capillary is held in a mechanical bracket that secures it by its outer diameter. The filament is floating in this configuration; it is free to translate along its length, but is constrained radially. It is secured on the non-reflective end by a simple mechanical clamp that is secured to a PZT. The PZT has a physical range of about 12 microns. This clamp/PZT assembly is then attached to a linear mechanical stage that allows much larger motions, driven by a micrometer with a digital readout. In this way, the filament can be coarsely positioned by hand to within about 10 microns. The PZT then has sufficient range and resolution to ensure the front face of the capillary and filament are co-planar. The fiber/capillary assembly and the assembly mounted with the PZT mechanism is shown below in Figure 3.

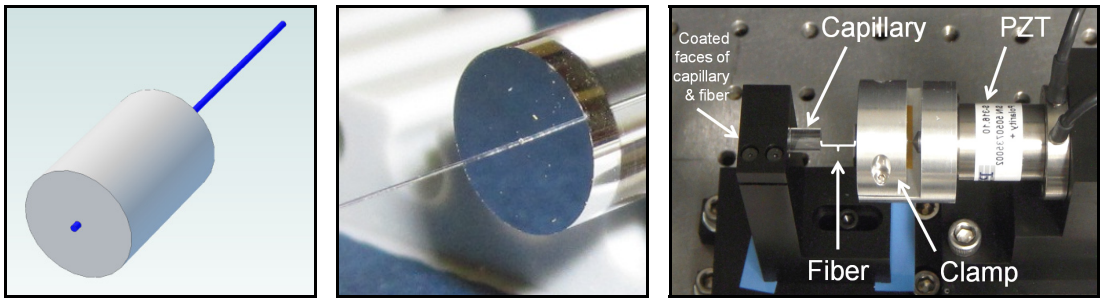

Figure 3. The focal plane assembly is shown in greater detail here. The image on the left is a schematic of our goal: a glass capillary tube with a fiber filament installed that is free to translate. The center image shows the optical assembly with a view of the mirrored surface of the capillary tube. The filament is installed and extends from the capillary to the lower left (its mirrored in the front face of the coated capillary). The image on the right is of the mounted filament/capillary assembly. The capillary mount is on the left, the PZT assembly is on the right. The coarse positioning stage is below the PZT mechanism and is not shown.

3.3 Testbed Opto/mechanical layout

An opto/mechanical layout of the experiment is shown below in Figure 4. The input beam is a from a single mode optical fiber. The fiber allows us to easily change the source between a laser and white light without any changes to the optical alignment. The beam is collimated with an off-axis paraboloid to ensure broadband operation. A fold mirror feeds the beam to a PZT tip/tilt mirror which is located at the input pupil. The phase aberrations are placed in the space between these two fold mirrors. Another fold mirror then directs the beam to the parabola. Our parabola is has a focal length of 914.4 mm, and we have a nominal input pupil diameter of 10 mm. The f/# is then f/91.44 and the Airy diameter is 2.44 λ f/# = 144.2 microns. The filament diameter is about 122 microns which corresponds to a width of 2.1 λ/D. The beam is relayed to the CCD camera with a simple pair of achromatic lenses. This lens relay magnifies the pupil by -0.4 such that the final pupil is 4 mm on the CCD. Our CCD is an SBIG ST-402ME with an array size of 765x510 and a pixel size of 9 microns. A photograph of the assembled hardware is shown in Figure 5.

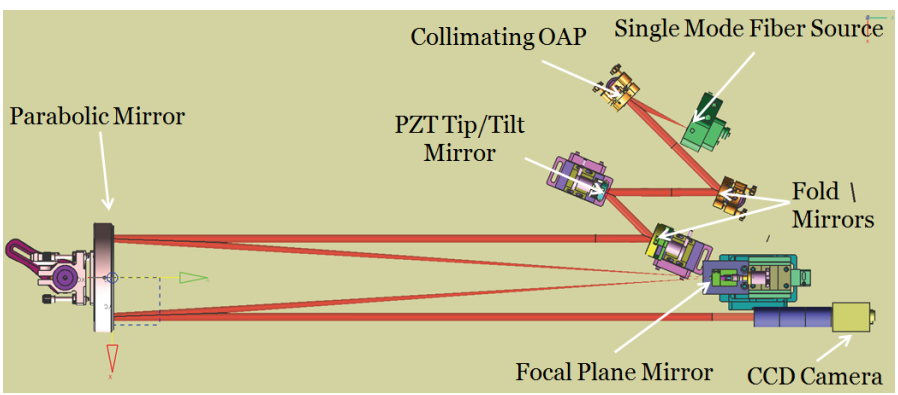

Figure 4. The opto/mechanical layout of the Zernike WFS testbed. The source is a single mode fiber which feeds and off-axis parabolic mirror which collimates the beam. The phase aberration is placed between the first fold mirror and the tip/tilt mirror. The tip/tilt mirror is at the location of the input pupil (the system is telecentric). The hardware at the intermediate focal plane is described above. The output pupil is imaged to the CCD with a lens relay that demagnifies the beam by -0.4.

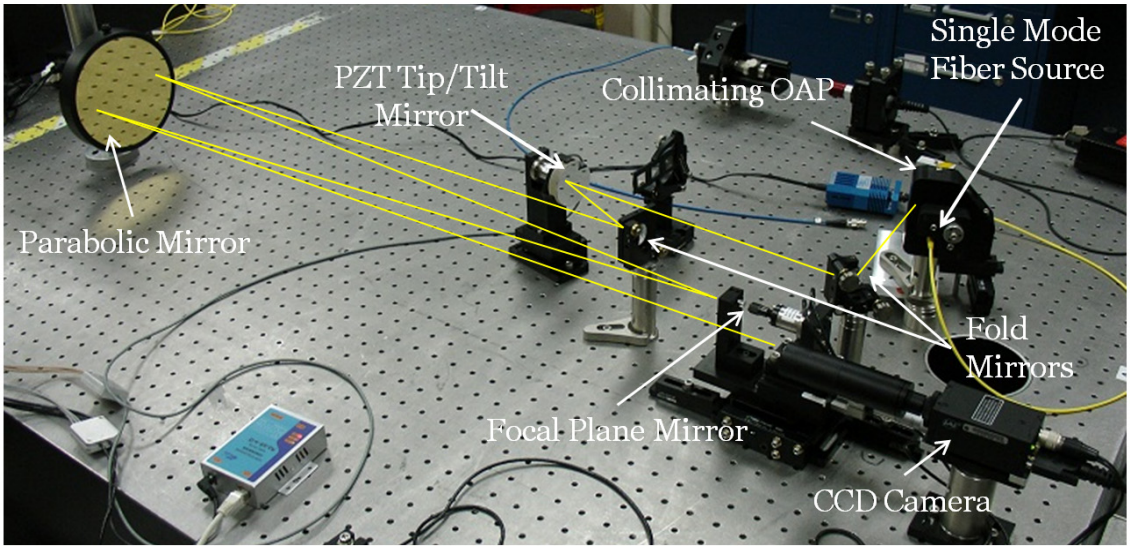

Figure 5. This photograph shows the hardware as installed on the optical table in the lab. It closely mirrors the opto/mechanical layout of the previous figure. We have installed an enclosure over this experiment to block ambient light and reduce air turbulence somewhat.

4. SIMULATIONS

4.1 Simulation outline

In order to analyze the performance of the Zernike wavefront sensor, an end-to-end simulation was constructed. The simulation has been used for three types of error analysis: Fourier mode analysis, and Zernike mode analysis.

In the simulation, phase errors are introduced into the electric field with uniform amplitude at the input pupil, and this modified electric field is propagated to the image plane. At the image plane, a mask corresponding to the lab filament size is applied to the electric field. In this way, a phase shift is applied only to the region of light incident on the fiber portion of the image plane. The shifted and unshifted portions of the electric field are recombined at the output pupil, where the intensities are used to calculate the phase (Equation 11).

4.2 Semi-Analytical Method of Fourier Transform

The Fourier transforms used to simulate the propagation of light between the pupil and image planes is calculated using the semi-analytical method (SAM). SAM provides a fast and memory efficient means of Fourier Transform between pupil and image planes in Lyot-style coronagraphs, introduced by Soummer[10]. In order to represent small features of the optical system, both the pupil and the image planes must be finely sampled, and the corresponding Fourier transform must be calculated using very large array sizes, creating demands on computer speed and memory efficiency. Unlike FFT methods, SAM removes the need for array padding, thus reducing the number of computations required to calculate the Fourier transform. By limiting the region of interest to a square array of side length N_A in the pupil plane and N_B in the image plane, the 2D Fourier transform of the function f(x,y) is computed by the matrix product:

$$F(u,v) = \frac{m}{N_A N_B} e^{-2i\pi ux^T} \cdot f(x,y) \cdot e^{-2i\pi yv^T}$$

where m is N_B divided by the scale factor •/D. The SAM and FFT methods yield numerically identical results over a range of input conditions, but SAM provides a speed improvement of about a factor of 35. Figure 6 compares the FFT and SAM methods at the input pupil, image plane, and output pupil.

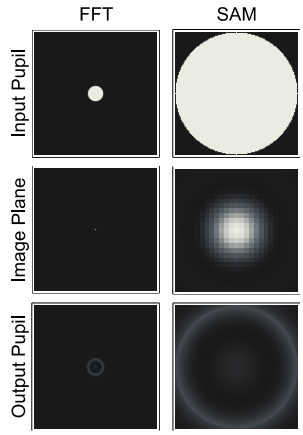

Figure 6. The results of the FFT and SAM methods are compared in the input pupil, image plane, and output pupil. Figure after Soummer et al 2007.The FFT array is heavily padded, while the SAM technique uses un-padded input and output pupils and calculates the FFT in only a restricted region of the focal plane.

As a means of verifying the numerical accuracy of the two techniques, we devised the following method: given a sinusoidal input phase, the maximum intensity at the image plane and output pupil was calculated over a range of phase amplitudes using both the FFT and SAM methods. The methods agree exactly over the amplitude range sampled.

4.3 Fourier Mode Analysis

The sensitivity of the Zernike WFS to Fourier modes was analyzed using a series of sinusoidal input phases with different spatial frequencies, or different numbers of cycles across the input pupil. A sinusoidal input phase introduced at the input pupil results in characteristic features at the image plane: two light spots are introduced above and below the PSF core. For lower spatial frequencies, these two spots are very close to the PSF core and about the size of the phase-shifting filament. As the spatial frequency increases, the spots move farther away from the PSF core, resulting in improved phase reconstruction. Figure 7 below demonstrates the relationship between the input phase spatial frequency, image plane features, phase reconstruction, and residual phase error.

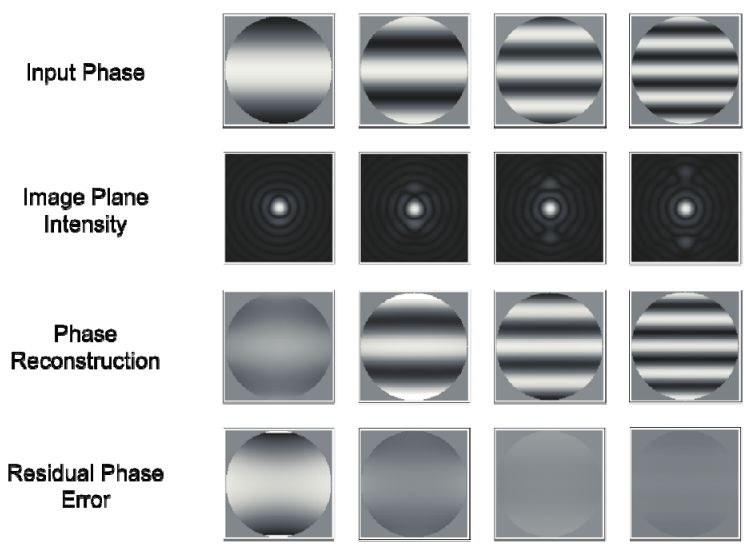

Figure 7. Sinusoidal input phase errors of different spatial frequencies result in characteristic light spots below and above the PSF core in the image plane. The phase reconstruction improves as the spots move away from the PSF core to higher spatial frequencies.

The results illustrated qualitatively by Figure 7 are shown quantitatively in Figure 8. Figure 8 demonstrates the improved phase reconstruction for higher spatial frequencies by plotting a reconstruction "phase scaling term."

This sensitivity parameter determines the magnitude of the input phase that is actually measured in the phase reconstruction algorithm. This parameter is determined as

$$\beta = \frac{\int \phi_{est} \cdot \phi_{input}}{\int \phi_{input} \cdot \phi_{input}} . \tag{13}$$

where the integrals are taken over the entire pupil. For a perfect phase reconstruction, the scaling term β goes to one. Figure 8 shows that β approaches one for high spatial frequencies.

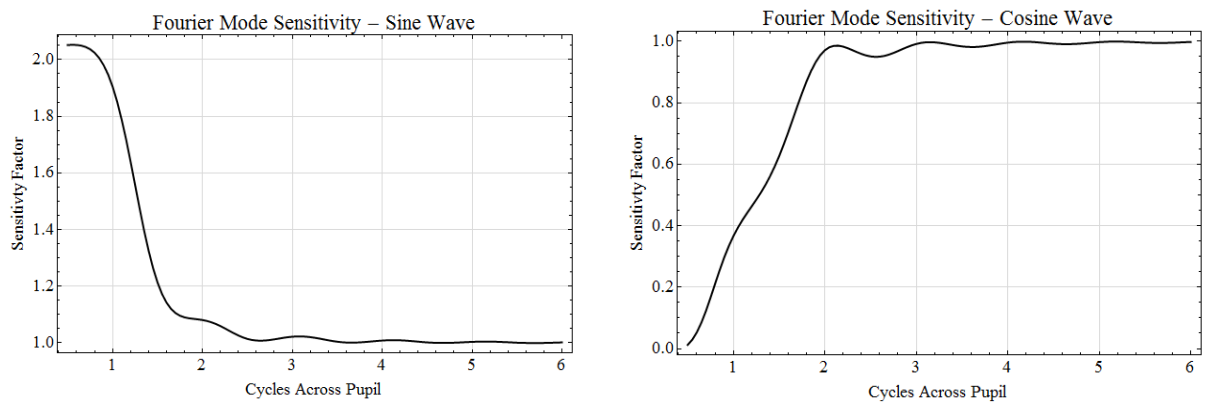

Figure 8. The phase reconstruction sensitivity factor β goes to one for higher spatial frequencies. We have analyzed both Sinusoidal and Co-sinusoidal waves of different spatial frequency across the pupil for a central piston element of size ~2 λ/D. For low-spatial frequency Sine waves, the ZWFS is super-sensitive, and actually over-estimates the phase error. For Cosine waves, the exact opposite is true. Low-spatial frequency cosine waves are underestimated by the ZWFS. The roll-off frequency however is roughly equal to the size of the phase shifting element (in λ/D units) in the focal plane.

4.4 Zernike Mode Analysis

The sensitivity of the simulated wavefront sensor to Zernike modes was first analyzed by calculating the residual phase error for five individual Zernike terms. As expected, first the wavefront sensor was found to be less sensitive to low Zernike modes and more sensitive to high Zernike modes. Figure 9 shows the input phase, image plane intensity, phase reconstruction, and residual phase error for Zernike terms 4, 5, 7, 9, and 10. Figure 10 confirms the sensitivity curve for the first 25 Zernike terms.

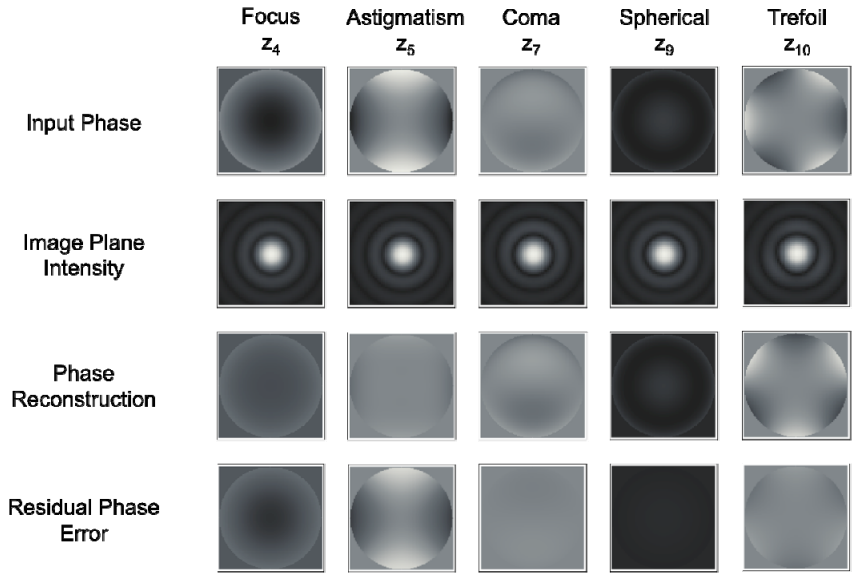

Figure 9. The input phase, image plane intensity, phase reconstruction, and residual phase error is shown for five Zernike terms. The error improves for higher Zernike terms.

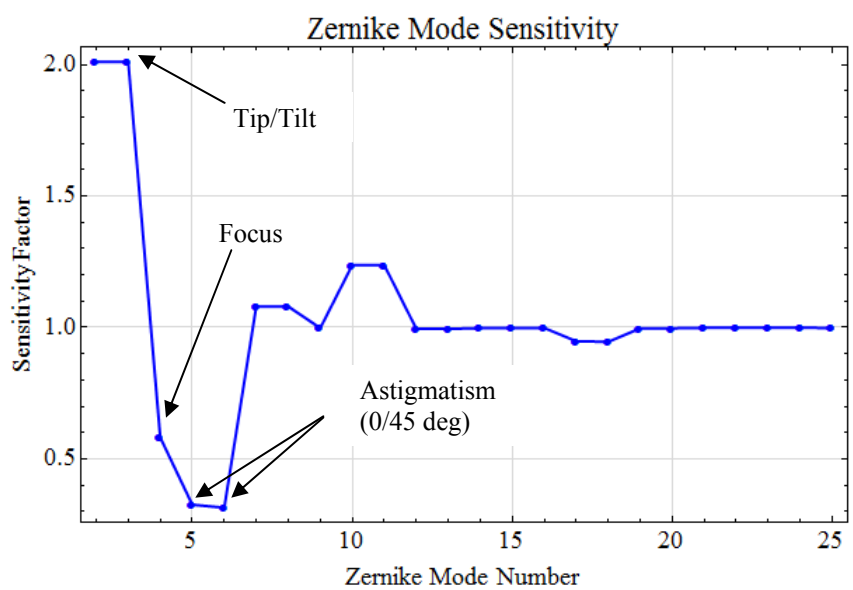

Figure 10. The phase reconstruction sensitivity factor, β, as a function of Zernike term is shown for the first twenty-five Zernike terms for a central piston element of size ~2 λ/D. Similar to the Sine wave analysis done for the Fourier Modes, the Zernike WFS is very sensitive to tip/tilt, but is less sensitive to low order modes. As the Zernike modes increase, the PSF energy moves to higher spatial frequencies and away from the phase-shifting element near the core of the PSF. The result is that the reconstructed phase gets progressively better.

5. SUMMARY AND CONCLUSION

The reflective, phase-shifting Zernike Wavefront Sensor as presented here has the same benefits as the original, static Zernike phase-contrast sensor in that it is simple, and common-mode. However, the dynamic phase-shifting capability also suppresses systematic noise sources like polarization variation, and the reflective design makes it insensitive to wavelength.

The sensitivity analysis for both the Zernike aberrations and Fourier modes indicates some insensitivity to low-order modes. However, knowledge of this can be used in post-processing to recover the low-order signals.

6. ACKNOWLEDGEMENTS

This work was carried out by the Jet Propulsion Laboratory, California Institute of Technology, under contract with the National Aeronautics and Space Administration. This work was supported by JPL's Research and Technology Development Fund. We would like to acknowledge Rosemary Diaz for her support in fabricating the fibers and making the capillary/fiber assemblies, Victor White for his support in etching the bare fibers down to size, and Randy Bartos for his support in the opto/mechanical layout of the experiment as well as his design and fabrication of the custom mechanical components. We also thank our fine vendors: Nu-Tek for the polishing capabilities, Coastline Inc. for the custom polishing and coatingn and for FiberGuide Industries for their fiber assemblies.

REFERENCES

[1] F. Zernike, "Das Phasenkontrastverfahren bei der Mikroskopischen beobachtung," Z. Tech. Phys. **16**, 454 (1935).
[2] F. Zernike, "Phasecontrast, a new method for the microscopic observation of transparent objects. Part I," Physica (Utrecht) **9** 686–698 (1942).
[3] F. Zernike, "Phasecontrast, a new method for the microscopic observation of transparent objects. Part II.," Physica (Utrecht) **9**, 974–986 (1942).
[4] F. Zernike, "How I discovered phase contrast," Science **121**, 345-349 (1955).
[5] R. Dicke, "Phase-Contrast Detection of Telescope Seeing and Their Correction", ApJ, 198, pp. 605-615 (1975).
[6] J. W. Goodman, *Introduction to Fourier Optics, 2nd Edition*, pp. 220-222 (McGraw-Hill, 1996).
[7] E. Hecht, *Opitcs, 4th Ed.*, p. 617-620, (Pearson Addison Wesley, 2002).
[8] D. Malacara, *Optical Shop Testing, 3rd Edition*, pp. 118-119 (Wiley-Interscience, 2007)
[9] E. Born and E. Wolf, *Principles of Optics, 6th Edition*, pp. 424-428 (Cambridge University Press, 1980).
[10] G.O. Reynolds, J.B. DeVelis, G.B. Parrent, B.J. Thompson, *The New Physical Optics Notebook: Tutorials in Fourier Optics*, pp. 475-477 (SPIE/AIP, 1989).
[11] R. Soummer, L. Pueyo, A. Sivaramakrishnan, and R. Vanderbei, "Fast computation of Lyot-style coronagraph propagation," Opt. Express 15, 15935-15951 (2007).